symmetry

MDPI

Article

CT Image Reconstruction via Nonlocal Low-Rank Regularization and Data-Driven Tight Frame

Yanfeng Shen [1,2,*], Shuli Sun [3], Fengsheng Xu [1], Yanqin Liu [1], Xiuling Yin [1] and Xiaoshuang Zhou [1]

[1] School of Mathematics and Big Data, Dezhou University, Dezhou 253023, China; xufengsheng@dzu.edu.cn (F.X.); liuyanqin@dzu.edu.cn (Y.L.); yinxiuling@dzu.edu.cn (X.Y.); zhongxiaoshuang@dzu.edu.cn (X.Z.)
[2] Data Recovery Key Laboratory of Sichuan Province, College of Mathematics and Information Science, Neijiang Normal University, Neijiang 641100, China
[3] Financial Department of Dezhou University, Dezhou 253023, China; sunshuli@dzu.edu.cn
* Correspondence: shenyanfeng@dzu.edu.cn; Tel.: +86-1876-600-1421

Abstract: X-ray computed tomography (CT) is widely used in medical applications, where many efforts have been made for decades to eliminate artifacts caused by incomplete projection. In this paper, we propose a new CT image reconstruction model based on nonlocal low-rank regularity and data-driven tight frame (NLR-DDTF). Unlike the Spatial-Radon domain data-driven tight frame regularization, the proposed NLR-DDTF model uses an asymmetric treatment for image reconstruction and Radon domain inpainting, which combines the nonlocal low-rank approximation method for spatial domain CT image reconstruction and data-driven tight frame-based regularization for Radon domain image inpainting. An alternative direction minimization algorithm is designed to solve the proposed model. Several numerical experiments and comparisons are provided to illustrate the superior performance of the NLR-DDTF method.

Keywords: Radon transform; image inpainting; nonlocal low-rank regularity; data-driven tight frame

MSC: 94A08; 42C15; 44A12; 68U10

Citation: Shen, Y.; Sun, S.; Xu, F.; Liu, Y.; Yin, X.; Zhou, X. CT Image Reconstruction via Nonlocal Low-Rank Regularization and Data-Driven Tight Frame. *Symmetry* **2021**, *13*, 1873. https://doi.org/10.3390/sym13101873

Academic Editor: Nikolai A. Sidorov

Received: 29 August 2021
Accepted: 28 September 2021
Published: 4 October 2021

1. Introduction

Medical imaging applications of X-ray computed tomography (CT) include cranial, chest, cardiac abdominal and pelvic imaging. The wide use of CT is due to the ability of viewing interior structures without destroying the surface of organs or subjects. However, the radiation caused by X-ray during imaging does harm to patients' health. Thus, the approximately lossless image reconstruction based on low-dose X-ray, such as reducing the number of projections, is continuously considered by scientists and doctors. The basic model of the X-ray reconstruction problem can be represented as a linear inverse problem,

$$Pu = f \tag{1}$$

where $P \in \mathbb{R}^{m\times n}$ is a projection operator representing the collection of discrete line integrations at different projection angles and along different beamlets. Numerically P is realized by Siddon's algorithm [1,2].

When small number of projections are used, i.e., $m < n$, the matrix P has a rank deficiency. As a result, Equation (1) will have an infinite amount of solutions. There are many methods for deriving a useful result from them, such as the solutions by the filtered back-projection (FBP) algorithm [3] and algebraic reconstruction technique (ART) [4]; however, they usually contain artifacts and thus result in unreliable reconstructions.

In practice, the projection image f usually contains noise. Gaussian noise [1,5–14] and Poisson noise [15,16] both are considered to simulate a realistic environment. Thus, the basic model (1) is modified by

$$f = Pu + \epsilon. \tag{2}$$

In order to suppress noise and artifacts (local irregularities) during image reconstruction, it should usually contain tiny structural or high-frequency information to maintain fidelity and effectiveness. Various differential operator-based regularization methods, such as the total variation (TV)-based regularization approach (see [6,7,15,17] and references therein), low-rank models (see [8,18]) and wavelet frame-based methods (see [9–12]), have been proposed and received acceptable results for both, in vision and computational error. A standard form of the TV-based image reconstruction model can be written as

$$\min_u \frac{1}{2}\|Pu - f\|_2^2 + \lambda\|\nabla u\|_1. \tag{3}$$

It is important to mention that the authors of [9] established a rigorous connection between a special model of wavelet frame-based approach, called the analysis-based approach, and variational models.

Two adjacent columns in the projected image f represent the information collected from adjacent projection angles. Therefore, f must be column-dependent locally. In order to exploit this kind of prior knowledge of f, the authors of [1] proposed an image inpainting method on the projection image f, following with another inverse problem for image restoration in the spatial domain. This wavelet frame-based regularity with Radon domain inpainting was shown to be useful for reconstructing high quality images from a very small number of projections,

$$\begin{aligned}\min_{f,u} \frac{1}{2}\|R_{\Lambda^c}(Pu - f)\|_2^2 + \frac{1}{2}\|R_\Lambda(Pu) - f_0\|_2^2 + \frac{\kappa}{2}\|R_\Lambda f - f_0\|_2^2 + \\ \lambda_1\|W_1 f\|_{1,2} + \lambda_2\|W_2 u\|_{1,2}.\end{aligned} \tag{4}$$

where R_{Λ^C} denotes the reconstruction on $\Omega\backslash\Lambda$, and R_Λ denotes the restriction on Λ. Here, f_0 is the projection image defined on the grid Λ of size $N_0 \times N_p$, where N_0 is the total number of detectors and N_p is the number of angular projections. The unknown projection image f is defined on a grid $\Omega \supset \Lambda$ of size $N_0 \times \widetilde{N}_p$, with $\widetilde{N}_p = 2N_p$ is selected in this paper. The first three terms of Equation (4) represent the data fidelity, making sure that f is consistent with f_0 on Λ and $Pf \approx f$. W_1 and W_2 are two different tight wavelet frame transforms. A fast algorithm was introduced to solve the model (4) based on the split Bregman algorithm [17,19,20] and the augmented Lagrangian method [21,22]. For more details about model and algorithm, we refer to [1].

Recently, it is known that in area of image restoration, data-driven tight frames or bi-frames generally outperform the regular pre-constructed wavelet frames [5,13,14]. The author of [5] proposed the SRD-DDTF model using data-driven tight frames as their sparsity priors for both u and f,

$$\begin{aligned}\min_{f,u,v_1,W_1,v_2,W_2} \frac{1}{2}\|R_{\Lambda^c}(Pu - f)\|_2^2 + \frac{1}{2}\|R_\Lambda(Pu) - f_0\|_2^2 + \frac{\kappa}{2}\|R_\Lambda f - f_0\|_2^2 + \\ \lambda_1\|v_1\|_0 + \frac{\mu_1}{2}\|W_1 f - v_1\|_2^2 + \lambda_2\|v_2\|_0 + \frac{\mu_2}{2}\|W_2 u - v_2\|_2^2, \\ \text{s.t. } W_i^T W_i = I,\ i = 1, 2.\end{aligned} \tag{5}$$

where tight frames W_1 and W_2 and corresponding coefficients v_1 and v_2, are all treated as unknowns for enforcing the sparsity approximation to u and f. Here, ℓ_0 norm $\|v_i\|_0$ stands for the number of non-zero elements in $v_i, i = 1, 2$. For solving the additional W_i and v_i subproblems such as Equation (7), an alternative optimization algorithm was proposed in [13] based on Singular Value Decomposition (SVD) of a matrix associated with the image

u (or f) after block rearrangement. As usual, the ℓ_0 regularization of v_i can be solved by applying hard-thresholding to the singular values. A short review is stated in Section 2.1, for more details and convergence analysis, we refer to [5,13,14].

It is desired that there exist lots of similar structures both in natural and medical images. This property of nonlocal self-similarity was introduced by Dong et al. in [23,24] for exploiting structured sparsity in compressive sensing of both photographic and CT/MRI images. Random sampling and pseudo-radial sub-sampling are used for under sampling. However, they did not use any inpainting method in the transform domain for reconstruction. Xie et al. [16] used the nonlocal self-similar constraint in the position emission tomography (PET) image reconstruction with Total Variation(TV) method. The nonlocal low-rank approximation and TV model were also used for reducing noise in the denoising problem of low-dose CT image [25]. Xu et al. [26] proposed a model based on nonlocal low-rank and prior images under a given wavelet framework for reducing limited-angle artifacts in CT image restoration. There are also many other applications of nonlocal low-rank methods in the field of image denoising, one may see [27] for details.

In this paper, the nonlocal patch-based method will be used for restoration of CT image u. Roughly speaking, we shall use low-rank approximation for several image block patches after block matching. The rest of this paper is organized as follows. In Section 2, we will review image restoration methods based on data-driven tight frame and nonlocal low-rank regularization. In Section 3, we shall introduce our CT image restoration model combining data-driven tight frames for f and nonlocal low-rank regularization for u. In Section 4, several experiments will be provided for validating the merits of our proposed method, and the conclusion is discussed in Section 5.

2. Reviews and Preliminaries

2.1. Data-Driven Tight Frames

In [1,5], the sparse approximation methods were proposed for both the CT image u and projection image f, which are based on the pre-constructed wavelet frames or data-driven tight frames. When implemented, the data-driven tight frames are constructed based on the SVD of a matrix associated with the image u (or f) after block rearrangement.

It is well known that compared with a basis, using a frame results in a more robust representation of signals [28,29]. In discrete setting, the fast decomposition transform W and fast reconstruction transform W^T, two finite matrix operators with entries from a filter $\{a_j\}_{j=0}^m$ associated to a translation-invariant tight wavelet transform, can be formed by convolution operators. Actually,

$$W^T = [S_{a_0}^T(-\cdot), S_{a_1}^T(-\cdot), \cdots, S_{a_m}^T(-\cdot)]^T \text{ and } W = [S_{a_0}, S_{a_1}, \cdots, S_{a_m}] \tag{6}$$

with convolution operator $S_a : \ell_2(\mathbb{Z}) \to \ell_2(\mathbb{Z})$,

$$[S_a u](n) = [a * u](n) = \sum_{k\in\mathbb{Z}} a(n-k)u(k) \text{ for } u \in \ell_2(\mathbb{Z}).$$

The tight frame property is guaranteed by $WW^T = I$ as usual, see [5]. The data-driven tight frame method takes the tight frame W as an unknown, which is also determined stepwisely by solving the following optimization problem:

$$\min_{v,W} \lambda\|v\|_0 + \|Wf - v\|_2^2, \;\; WW^T = I. \tag{7}$$

We also use a small-size W, thus, the phantom image f should be reshaped as the matrix $F \in \mathbb{R}^{(N_1N_2)\times p}$. Here, each column is a vectorization of $N_1 \times N_2$ patches extracted from f. The filters $\{a_j\}_{j=0}^m$ used for W are selected as the columns of the matrix $D \in$

$\mathbb{R}^{(N_1N_2)\times m}$. By denoting $V \in \mathbb{R}^{(N_1N_2)\times p}$ as the tight frame coefficients and taking $m = N_1N_2$, Equation (7) can be rewritten as

$$\min_{V,D} \lambda\|V\|_0 + \|D^TF - V\|_2^2, \quad D^TD = I. \tag{8}$$

In the sequel, we follow the alternative optimization algorithm for solving Equation (8), see [5,13] for details,

$$\begin{cases} D^{k+1} = XY^T \\ V^{k+1} = T_\lambda\left((D^{k+1})^TF\right) \end{cases} \tag{9}$$

with X and Y obtained by taking SVD of $F(V^k)^T$, and T_λ being the hard-thresholding operator defined by

$$(T_\lambda V)[i,j] = \begin{cases} 0, & \text{if } |x| < \lambda \\ \{0, V[i,j]\}, & \text{if } |x| = \lambda \\ V[i,j], & \text{otherwise.} \end{cases} \tag{10}$$

2.2. Nonlocal Low-Rank Regularization

The nonlocal low-rank regularization is used for compressed sensing [24], PET image reconstruction [16] and CT image restoration from limited-angle projection data [26]. All these problems are handled by the alternative direction multiplier method technique, which is converted into several sub-problems and solved iteratively and alternately. When implemented, the rank-minimization sub-problem is also solved by the singular value thresholding (SVT) method, and the image reconstruction sub-problem is solved by different regularization methods.

In this article, the nonlocal low-rank regularization is used for CT image restoration, for the purpose of exploiting the nonlocal property in the image. After extracting $\sqrt{n_1} \times \sqrt{n_1}$ patches at position i in CT image u, denoted by $x_i \in \mathbb{R}^{n_1}$, m_1-nearest patches based on Euclidean distance are used for obtaining the matrix $X_i = [x_{i,0}, x_{i,1}, \cdots, x_{i,m_1-1}]$. Here, each $x_{i,r}$ is its reordered position index, satisfying $S_i = \{r|\|x_i - x_{i,r}\| \leq T_i\}$ and T_i is the pre-defined threshold.

Since in the natural image there exist lots of nonlocal self-similar structures, the formed data X_i can be split into two parts, the low-rank matrix L_i and the Gaussian noise matrix W_i, i.e., $X_i = L_i + W_i$. Then, L_i can be recovered by the low-rank regularization model,

$$L_i = \underset{L_i}{\operatorname{argmin}} \operatorname{Rank}(L_i), s.t. \|X_i - L_i\|_2^2 \leq \sigma_W^2, \tag{11}$$

where σ_W^2 denotes the variance of Gaussian noise. In order to solve Equation (11), as in [24], we consider an approximate version,

$$L_i^{k+1} = \underset{L_i}{\operatorname{argmin}} \|X_i - L_i\|_2^2 + \lambda_2\phi(L_i, \sigma_\epsilon^k), \tag{12}$$

where $\phi(L_i, \sigma_\epsilon^k) = \sum_{r=0}^{n_0} \sigma_{\epsilon,r}^k\sigma_r$ denotes the weighted nuclear norm with $\sigma_{\epsilon,r}^k = \frac{1}{\sigma_r^k+\epsilon}$ and $n_0 = \min\{n_1, m_1\}$. The singular values σ_r and σ_r^k corresponding to L_i and L_i^k, respectively, are ordered in descending order. We adopt the weighted singular value thresholding method to solve Equation (12) efficiently and effectively,

$$L_i^{k+1} = S_{\sigma_\epsilon^k}(X_i) = U\left(\Sigma - \lambda_2 \operatorname{diag}(\sigma_\epsilon^k)\right)_+ V^T, \tag{13}$$

where $U\Sigma V^T$ is the SVD of X_i, $(x)_+ = \max\{x, 0\}$ and $\sigma_\epsilon^k = \left[\frac{1}{\sigma_1^k+\epsilon}, \frac{1}{\sigma_2^k+\epsilon}, \cdots, \frac{1}{\sigma_{n_0}^k+\epsilon}\right]$.

3. Models and Algorithm

3.1. CT Image Reconstruction Model

In this paper, we also focus on the column number of the unknown projection image satisfying $\widetilde{N}_p = 2N_p$, with N_p being the column number of f_0. f is considered to be restored from f_0 with doubled angular sampling resolution. Unlike the symmetric model (5), we use nonlocal low-rank regularization instead of the data-driven tight frame method when dealing with CT images. Our asymmetric CT image reconstruction model based on nonlocal low-rank regularity and data-driven tight frames reads as follows,

$$\min_{u,f,W,v,L_i} \frac{1}{2}\|R_{\Lambda^C}(Pu-f)\|_2^2+\frac{1}{2}\|R_\Lambda Pu-f_0\|_2^2+\frac{\kappa}{2}\|R_\Lambda f-f_0\|_2^2+ \lambda_1\|v\|_0+\frac{\mu}{2}\|Wf-v\|_2^2+\eta\sum_j\left\{\frac{1}{2}\|\widetilde{R}_i u-L_i\|_2^2+\lambda_2\phi(L_i,\sigma_\epsilon^k)\right\} \tag{14}$$

where $\widetilde{R}_i u = \left[R_{i,0}u, R_{i,1}u, \cdots, R_{i,m_1-1}u\right]$ denotes the first m_1 closest patches under cosine similarity for every exemplar patch x_i. In this section, we demonstrate that the proposed objective functional can be efficiently solved by the method of alternative minimization. After k-th iteration, the variables of step $k+1$ are determined by the following sub-problems.

(1) f sub-problem

If all the parameters but f are determined by k-th iteration, Equation (14) can be practically rewritten as

$$f^{k+1} = \operatorname*{argmin}_f \frac{1}{2}\|R_{\Lambda^C}(Pu-f)\|_2^2+\frac{\kappa}{2}\|R_\Lambda f-f_0\|_2^2+\frac{\mu}{2}\|W^k f-V^k\|_2^2+\frac{a}{2}\|f-f^k\|_2^2. \tag{15}$$

Here, we add a special term$\|f-f^k\|_2^2$ in order to ensure that the new f^{k+1} is not far from f^k, which can theoretically justify the convergence of this algorithm. By differentiating the right side of Equation (15) with respect to f, we obtain the following closed-form solution

$$f^{k+1} = [R_{\Lambda^C}+\kappa R_\Lambda+(\mu+a)]^{-1}(R_{\Lambda^C}Pu^k+\kappa R_\Lambda f_0+\mu {W^k}^T V^k+af^k), \tag{16}$$

where $[R_{\Lambda^C}+\kappa R_\Lambda+(\mu+a)]$ is a diagonal matrix and, hence, Equation (16) can be computed easily.

(2) W and v sub-problem

In this paper, we use the data-driven tight frame method explained in [5] or Section 2, for W and v sub-problems,

$$W^{k+1} = \operatorname*{argmin}_{W^TW=I} \frac{\mu}{2}\|Wf^{k+1}-v^k\|_2^2+\frac{c}{2}\|W-W^k\|_2^2$$

$$v^{k+1} = \operatorname*{argmin}_v \frac{\mu}{2}\|W^{k+1}f^{k+1}-v\|_2^2+\lambda_1\|v\|_0+\frac{d}{2}\|v-v^k\|_2^2$$

As discussed in the previous section, the variables f, v and W are reformulated in the practice calculation. To be more specific, we need to solve the following reformulated sub-problems:

$$D^{k+1} = \operatorname*{argmin}_{D^TD=I} \frac{\mu}{2}\|D^TF^{k+1}-V^k\|_2^2+\frac{c}{2}\|D-D^k\|_2^2 \tag{17}$$

$$V^{k+1} = \operatorname*{argmin}_V \frac{\mu}{2}\|(D^{k+1})^TF^{k+1}-V\|_2^2+\lambda_1\|V\|_0+\frac{d}{2}\|V-V^k\|_2^2 \tag{18}$$

Thus, to solve sub-problems (17) and (18), we can simply compute

$$D^{k+1} = XY^T \text{ where } X\Sigma Y^T = F^{k+1}(V^{k+1})^T + \frac{c}{\mu}D^k \tag{19}$$

and

$$V^{k+1} = \mathrm{T}_{\sqrt{\frac{\lambda_1}{\mu+d}}}\left(\frac{\mu(D^{k+1})^T F^{k+1} + dV^k}{\mu + d}\right), \tag{20}$$

where $T_a(\cdot)$ is the hard thresholding operator given in Equation (10).

(3) L_i and u sub-problems

Based on the augmented Lagrangian method, we formulate the L_i sub-problem as,

$$L_i^{k+1} = \underset{L_i}{\operatorname{argmin}} \frac{1}{2}\|\widetilde{R}_i u^k - L_i\|_2^2 + \lambda_2 \phi(L_i, \sigma_\epsilon^k) + \frac{e}{2}\|L_i - L_i^k\|_2^2 \tag{21}$$

with $\phi(L_i, \sigma_\epsilon^k) = \sum_{r=1}^{n_0} \frac{\sigma_r}{\sigma_r^k + \epsilon}$. Here, σ_r and σ_r^k are the r-th ordered singular value with respect to L_i and L_i^k. Applying the weighted singular value thresholding operator to Equation (21) yields the algorithm

$$L_i^{k+1} = S_{\sigma_\epsilon^k}\left(\widetilde{R}_i u^k + eL_i^k\right) = U\left(\widetilde{\Sigma} - \frac{\lambda_2}{1+e}\operatorname{diag}(\sigma_\epsilon^k)\right)_+ V^T \tag{22}$$

where $U\widetilde{\Sigma}V^T$ is the SVD of $\widetilde{R}_i u^k + eL_i^k$.

After L_i being updated, the current estimation of CT image u can be solved by our proposed model with other variables fixed,

$$u^{k+1} = \underset{u}{\operatorname{argmin}} \frac{1}{2}\|R_{\Lambda^C} Pu - f^{k+1}\|_2^2 + \frac{1}{2}\|R_\Lambda Pu - f_0\|_2^2 + \frac{\eta}{2}\sum_k \|\widetilde{R}_i u - L_i^{k+1}\|_2^2 + \frac{b}{2}\|u - u^k\|_2^2, \tag{23}$$

where the term $\|u - u^k\|_2^2$ stands for the similarity in two adjacent steps. It is a quadratic optimization problem admitting a closed-form solution,

$$u^{k+1} = \left[P^T P + \eta\sum_i \widetilde{R}_i^T \widetilde{R}_i + bI\right]^{-1}\left[P^T R_{\Lambda^C} f^{k+1} + P^T R_{\Lambda^C} f_0 + \eta\sum_i \widetilde{R}_i^T L_i^{k+1} + bu^k\right],$$

where $\widetilde{R}_i^T L_i^{k+1} = \sum_{r=0}^{m-1} R_{i,r}^T L_{i,r}^{k+1}$ and $\widetilde{R}_i^T \widetilde{R}_i = \sum_{r=0}^{m-1} R_{i,r}^T R_{i,r}$ is a diagonal matrix. In order to derive a much faster algorithm for solving Equation (23), we also use the alternative direction multiplier method (ADMM) [30]. Thus, we obtain

$$\begin{aligned} u^{k+1} = \underset{u}{\operatorname{argmin}} \frac{1}{2}\|R_{\Lambda^C} Pu - f^{k+1}\|_2^2 + \frac{1}{2}\|R_\Lambda Pu - f_0\|_2^2 + \frac{b}{2}\|u - u^k\|_2^2 \\ + \frac{\beta}{2}\|u - z + \frac{\mu}{\beta}\|_2^2 + \frac{\eta}{2}\sum_i \|\widetilde{R}_i z - L_i^{k+1}\|_2^2, \end{aligned} \tag{24}$$

where $z \in \mathbb{R}^{n\times n}$ is an auxiliary variable, $u \in \mathbb{R}^{n\times n}$ is the Lagrangian multiplier, and β is a positive scalar parameter. The split iteration version of the optimization of Equation (24) can be stated as follows:

$$
\begin{aligned}
z^{k+1} &= \underset{z}{\operatorname{argmin}} \frac{\beta^k}{2}\|u^k - z + \frac{\mu^k}{\beta^k}\|_2^2 + \frac{\eta}{2}\sum_i \|\widetilde{R}_i z - L_i^{k+1}\|_2^2 \\
u^{k+1} &= \underset{u}{\operatorname{argmin}} \frac{1}{2}\|R_{\Lambda^C} P u - f^k\|_2^2 + \frac{1}{2}\|R_\Lambda P u - f_0\|_2^2 + \frac{b}{2}\|u - u^k\|_2^2 + \frac{\beta^k}{2}\|u - z^{k+1} + \frac{\mu^k}{\beta^k}\|_2^2 \\
\mu^{k+1} &= \mu^k + \beta^k(\mu^k - z^{k+1}) \\
\beta^{k+1} &= 1.2\beta^k.
\end{aligned}
$$

Here, z^{k+1} admits a closed-form solution,

$$
z^{k+1} = \left[\eta \sum_i \widetilde{R}_i^T \widetilde{R}_i + \beta^k I\right]^{-1} \left[\beta^k u^k + \mu^k + \eta \sum_i \widetilde{R}_i^T L_i^{k+1}\right],
$$

$\sum_i \widetilde{R}_i^T \widetilde{R}_i$ is a diagonal matrix with each diagonal element being the number of overlapping patches that cover the current pixel location. $\sum_i \widetilde{R}_i^T L_i^{k+1}$ denotes the weighted low-rank approximation, i.e., gathering useful information from the collected similar patches.

For u^{k+1}, we also use the conjugate gradient method to solve a linear equation,

$$
\left[P^T P + (b + \beta^k) I\right] u = P^T R_{\Lambda^C} f^{k+1} + \mu^k + \eta \sum_i \widetilde{R}_i^T L_i^{k+1}
$$

Collecting all together, we derive the following Algorithm 1.

Algorithm 1: CT image reconstruction via nonlocal low-rank regularity and data-driven tight frame (NLR-DDTF).

1 **Input:** compute u^0 from (5) and set $f^0 = Pu^0$. Compute v^0, w^0 from (4).
2 **Repeat:**
3 (1): update f^{k+1} by optimizing f using (16)
4 (2): update D^{k+1} and V^{k+1} by (19) and (20)
5 (3): update L_i^{k+1},for all i using (22)
6 (4): update u^{k+1} by solving (24)
7 **Until:** Relative error $\|u^{k+1} - u^k\| / \|u^{k+1}\| < \epsilon$
8 **Output:** u^k

4. Experiments

In this section, we report the experimental results of the proposed asymmetric low-rank approximation and data-driven tight frame-based asymmetric CT image recovery method. The proposed joint regulation method is actually based on the SRD-DDTF model [5]. The major difference is the optimization method for updating u^k. Thus, we select the same warm-started initial value u^0 as in [5], given by analysis of the model in Section 3.1. In the following, we consider three phantoms, head image with smaller details from [5], head image and brain image with much more details from [24]. All experiments are conducted on a 3.20 GHZ Intel(R) Core(TM) i7-8700cpu with 16 GB memory. The PSNR, relative error and correlation results of the reconstructed images are included in Table 1, additionally, the visual effects are reported in Figures 1–3. Both of them reveal that the nonlocal low-rank method does preserve more information from the underground truth other than noise, which contains less structural information.

The degrade projection image f_0 is constructed by the every-other-angular extraction method from synthesized data, based on the Radon transform of real data u and the Monte Carlo simulation, $f_0 = R_\Lambda(Pu + \epsilon)$, where ϵ is some Gaussian white noise and

the projection number N_p is considered to be $15, 30, 45, 60$ in all examples. We choose the standard deviation of noise as $\max(|Pu|)/300$ in our experiments. The projection image f is calculated based on the photon numbers the detectors received. Gaussian white noise is also generated when the corresponding optical equipment counts photons, which is related to the uncertainty of photons. For an initial value of f, we directly use Pu^0 as in [5].

The patch size for u is 6×6 and the patch size for f is 8×2 to adapt to the different shape of u and f. For optimization of the W and v subproblems, we use $\mu = 8400\lambda_1$ and λ_1 is selected the same as in the SRD-DDTF model (5). When splitting the image u into overlapped small patches, we extract a paragon patch in every N_s pixels along both horizontal and vertical directions. Here, we use $N_s = 5$ and $N_s = 3$ for realizing our proposed NLR-DDTF model. For each patch of u, $m_1 = 41$ similar patches are selected when the low-rank approximation is executed to derive L_i. In our application, we choose $\eta = 0.8$ for smaller details in the image "head1" and $\eta = 1.6$ for the many more details in images "head2" and "brain". The regularization parameter λ_2 is selected to be 1.

For quantitative accuracy evaluation, the relative error and correlation for the reconstructed u corresponding to the ground truth image u_t are defined as:

$$err(u_t, u) = \frac{\|u - u_t\|_2}{\|u_t\|_2} \text{ and } corr(u_t, u) = \frac{(u - \overline{u})(u_t - \overline{u}_t)}{\|u - \overline{u}\|_2 \|u_t - \overline{u}_t\|_2}$$

with $\overline{u}$ and $\overline{u}_t$ being the mean of u and u_t. The maximum iteration number of all our experiments is set to 1000 with the following stopping criterion: whenever the relative change between two consecutive iterations is below 10^{-3} (or 10^{-4} for "head1" with higher N_p than 15).

Table 1. Comparison of relative errors (in percentage), correlations (in percentage), PSNR (in db) and running time (in seconds). For image "head1", NLR-DDTF methods can improve PSNR 3.8–27.2% with consuming 15.7–240.2% more time; For image "head2", NLR-DDTF methods can improve PSNR 0.2–24.6% with consuming 29.1–233.7% more time; for image "brain", NLR-DDTF methods can improve PSNR 1.3–11.0% with consuming 18.9–225.7% more time.

"head1"

N_p	SRD-DDTF				NLR-DDTF with $N_s = 5$				NLR-DDTF with $N_s = 3$			
	err	corr	psnr	time	err	corr	psnr	time	err	corr	psnr	time
15	10.50	99.06	35.81	470.60	8.97	99.13	37.16	860.71	8.10	99.44	38.03	1600.87
30	5.40	99.75	41.57	923.97	2.03	99.96	50.05	1251.05	1.93	99.97	50.50	1937.15
45	4.28	99.84	43.58	1367.35	1.28	99.96	54.05	1672.66	1.22	99.987	54.48	2368.40
60	3.80	99.88	44.61	1809.70	0.98	99.99	56.38	2095.44	0.941	99.992	56.74	2782.54

"head2"

N_p	SRD-DDTF				NLR-DDTF with $N_s = 5$				NLR-DDTF with $N_s = 3$			
	err	corr	psnr	time	err	corr	psnr	time	err	corr	psnr	time
15	29.38	92.34	22.47	495.41	29.21	92.39	22.52	888.51	29.22	92.39	22.52	1653.06
30	20.71	96.28	25.51	914.76	15.66	97.87	27.93	1284.95	15.44	97.93	28.05	1953.55
45	16.94	97.54	27.25	1378.70	10.04	99.13	31.80	1718.87	9.90	99.15	31.91	2443.62
60	15.37	97.98	28.09	1773.86	7.01	99.58	34.91	2290.07	6.939	99.58	35.00	2861.41

"brain"

N_p	SRD-DDTF				NLR-DDTF with $N_s = 5$				NLR-DDTF with $N_s = 3$			
	err	corr	psnr	time	err	corr	psnr	time	err	corr	psnr	time
15	23.87	95.51	28.73	476.95	22.87	95.88	29.10	909.44	22.50	96.02	29.24	1553.29
30	15.57	98.12	32.44	944.79	12.34	98.82	34.46	1284.81	12.09	98.87	34.63	2059.53
45	12.97	98.70	34.03	1390.10	9.31	99.33	36.91	1728.38	9.22	99.34	36.99	2453.39
60	11.60	98.96	35.00	1777.77	7.51	99.56	38.77	2112.93	7.45	99.57	38.84	2838.36

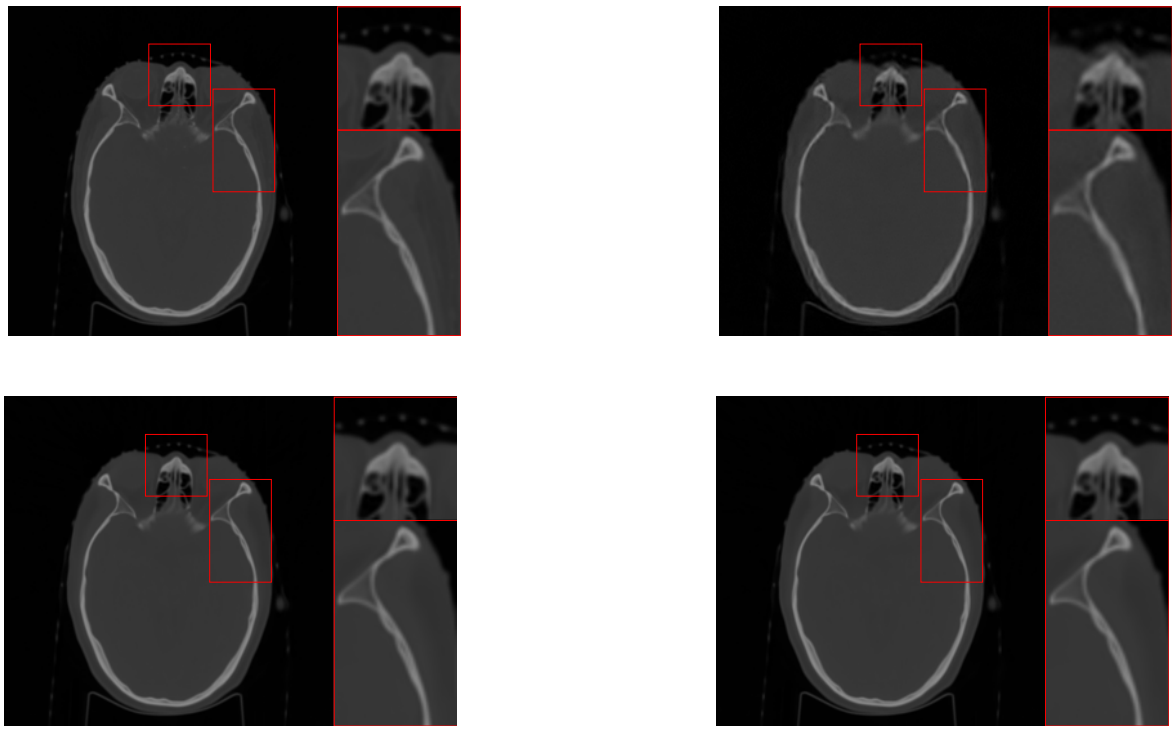

Figure 1. The tomographic results for the image "head1". (**top left**) True data and local detail area for comparison; (**top right**) the restored image by SRD-DDTF method [5]; (**bottom left**) the restored image by NLR-DDTF method with $N_s = 5$; (**bottom right**) the restored image by NLR-DDTF method with $N_s = 3$.

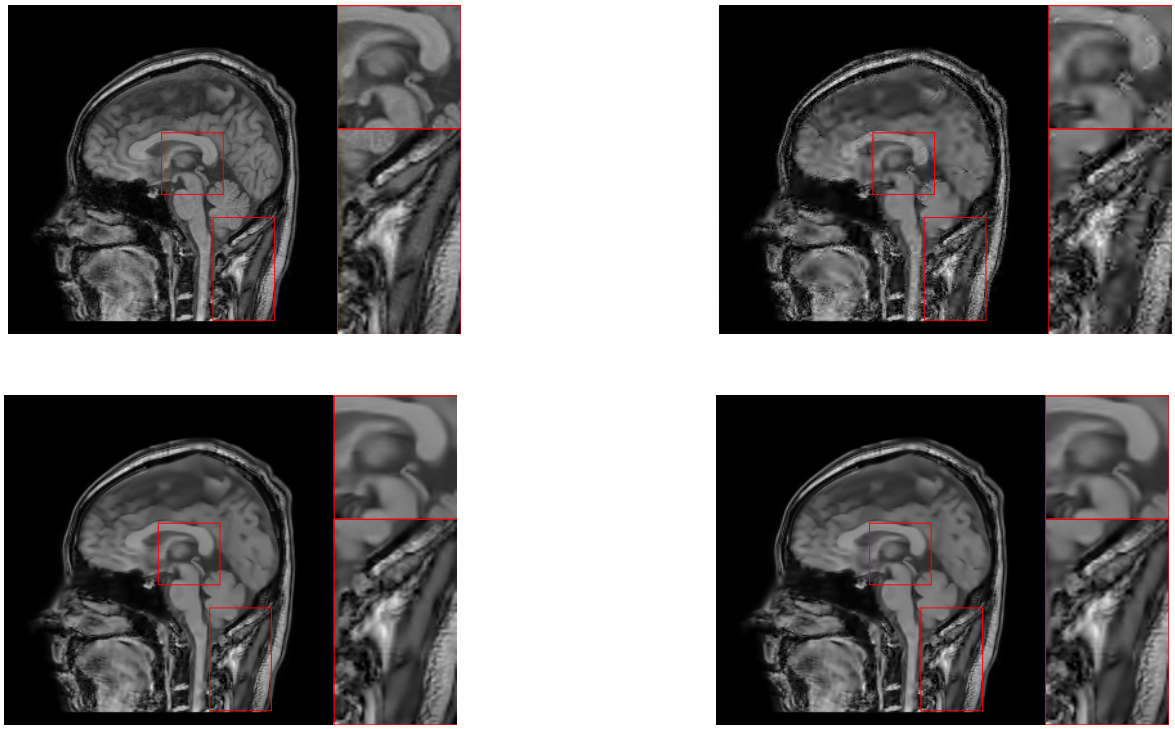

Figure 2. The tomographic results for the image "head2". (**top left**) True data and local detail area for comparison; (**top right**) the restored image by SRD-DDTF method [5]; (**bottom left**) the restored image by NLR-DDTF method with $N_s = 5$; (**bottom right**) the restored image by NLR-DDTF method with $N_s = 3$.

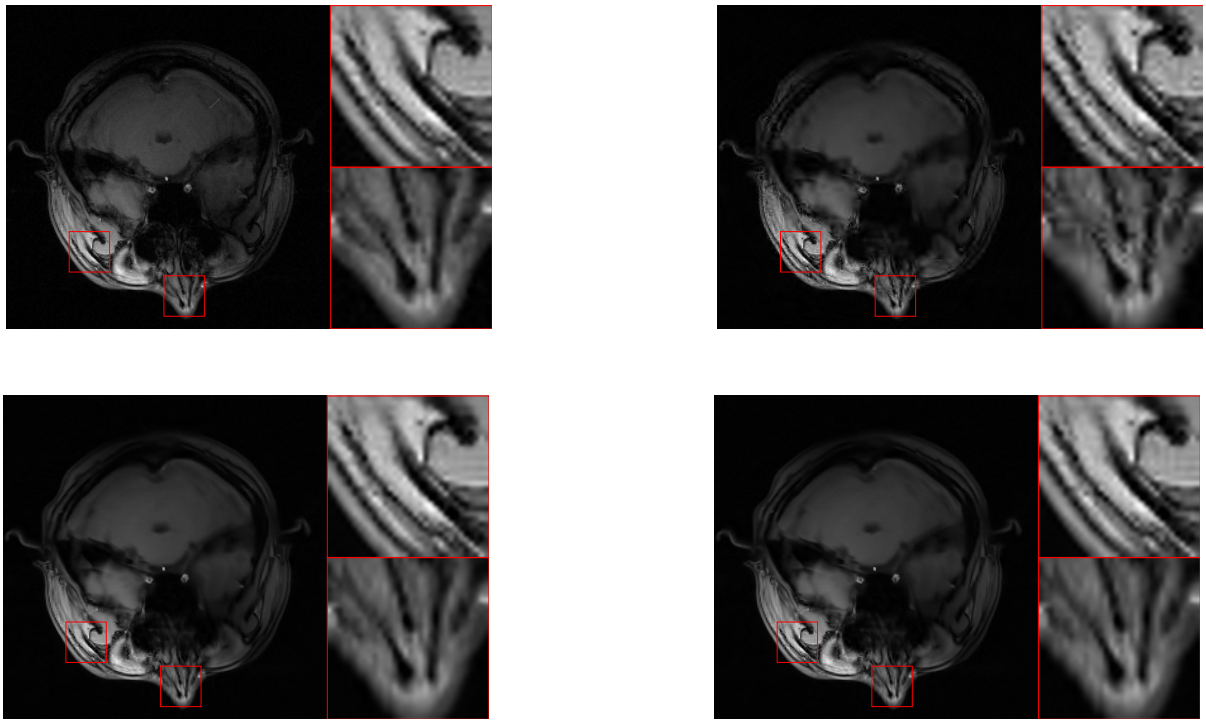

Figure 3. The tomographic results for the image "brain". (**top left**) True data and local detail area for comparison; (**top right**) the restored image by SRD-DDTF method [5]; (**top right**) the restored image by NLR-DDTF method with $N_s = 5$; (**bottom right**) the restored image by NLR-DDTF method with $N_s = 3$.

5. Conclusions

In this work, we introduced a novel spatial-Radon domain CT image reconstruction model, which combines the spatial domain inverse problem based on the nonlocal low-rank approximation method and the Radon domain inpainting model using a data-driven tight frame-based regularization. The proposed model reconstructs high quality and high resolution CT images even when the images contain more details than the observed low-resolution projection images. We used the split Bregman algorithm for numerical simulations of the proposed model.

The success of the regularization method in CT image restoration, no matter TV-based or wavelet frame-based, lies in the property of local smoothness or structure sparsity of the ground truth image. It is shown in [5] that using data-driven tight frame as sparsity priors for Radon domain projection image preformed better than using pre-determined wavelet frame systems. The nonlocal low-rank prior can reflect the group sparsity characteristic of similar patches in CT images well. Our proposed CT image restoration method combines the advantages of the above two methods. The PSNR and subjective quality comparison shown in Table 1 clearly reveal that the proposed NLR-DDTF method performs better than just the tight frame in several cases. Compared with the SRD-DDTF method, our proposed NLR-DDFT model's shortcoming is the slightly higher time consumption. When $N_s = 5$, the average time required for all examples is 42% longer, and the average time consumption is 120% times higher if $N_s = 3$.

Author Contributions: Models, methodology and formal analysis, Y.S. and S.S.; conceptualization and data curation, F.X.; convergence and supervision, Y.L.; programming and experiments, Y.S. and F.X.; writing—original draft preparation, Y.S. and S.S.; writing—review and editing, Y.L., X.Y. and X.Z.; project administration, F.X., Y.L. and X.Y. All authors have read and agreed to the published version of the manuscript.

Funding: This research was funded by Science and Technology Research Program for Universities in Shandong Province, China (Grant No. J16LI58 and J18KB099), Natural Science Foundation of Shandong Province (Grant No. ZR2018LA003), Open Research Fund Program of Data Recovery Key Laboratory of Sichuan Province (Grant No. DRN19020), National Natural Science Foundation of China (No. 11801060, 11501082) and Research and Development Project of Dezhou City in China.

Acknowledgments: The authors would like to thank B. Dong and W. Dong for providing the test images and source code used in the simulation experiments.

Conflicts of Interest: The authors declare no conflict of interest. The funders S.Y., L.Y. and Y.X. had a role in the design of the study, in the analyses and interpretation of data, in the writing of the manuscript, and in the decision to publish the results.

References

1. Dong, B.; Li, J.; Shen, Z. X-ray ct image reconstruction via wavelet frame based regularization and radon domain inpainting. *J. Sci. Comput.* **2013**, *54*, 333–349. [CrossRef]
2. Siddon, R. Fast calculation of the exact radiological path for a three-dimensional CT array. *Med. Phys.* **1985**, *12*, 252. [CrossRef] [PubMed]
3. Feldkamp, L.; Davis, L.; Kress, J. Practical cone-beam algorithm. *J. Opt. Soc. Am. A* **1984**, *1*, 612–619. [CrossRef]
4. Gordon, R.; Bender, R.; Herman, G. Algebraic reconstruction techniques (ART) for three-dimensional electron microscopy and X-ray photography. *J. Theor. Biol.* **1970**, *29*, 471–481. [CrossRef]
5. Zhan, R.; Dong, B. CT image reconstruction by spatial-Radon domain data-driven tight frame regulatization. *SIAM J. Imaging Sci.* **2016**, *9*, 1063–1083. [CrossRef]
6. Rudin, L.; Osher, S.; Fatemi, E. Nonlinear total variation based noise removal algorithms. *Phys. D Nonlinear Phenom.* **1992**, *60*, 259–268. [CrossRef]
7. Sidky, E.; Pan, X. Image reconstruction in circular cone-beam computed tomography by constrained, total-variation minimization. *Phys. Med. Biol.* **2008**, *53*, 4777. [CrossRef]
8. Cai, J.; Candes, E.; Shen, Z. A singular value thresholding algorithm for matrix completion. *SIAM J. Optim.* **2010**, *20*, 1956–1982. [CrossRef]
9. Cai, J.; Dong, B.; Osher, S.; Shen, Z. Image restorations: Total variation, wavelet frames and beyond. *J. Am. Math. Soc.* **2012**, *25*, 1033–1089. [CrossRef]
10. Cai, J.; Dong, B.; Shen, Z. Image restorations: A wavelet frame based model for piecewise smooth functions and beyond. *Appl. Comput. Harmon. Anal.* **2016**, *41*, 94–138. [CrossRef]
11. Dong, B.; Jiang, Q.; Shen, Z. Image Restoration: Wavelet Frame Shrinkage, Nonlinear Evolution PDEs, and Beyond. *Multiscale Model. Simul.* **2017**, *15*, 606–660. [CrossRef]
12. Dong, B.; Shen, Z.; Xie, P. Image restoration: A general wavelet frame based model and its asymptotic analysis. *SIAM J. Math. Anal.* **2017**, *49*, 421–445. [CrossRef]
13. Cai, J.; Ji, H.; Shen, Z.; Ye, G. Data-driven tight frame construction and image denoising. *Appl. Comput. Harmon. Anal.* **2014**, *37*, 89–105. [CrossRef]
14. Bao, C.; Ji, H.; Shen, Z. Convergence analysis for iterative data-driven tight frame construction scheme. *Appl. Comput. Harmon. Anal.* **2015**, *38*, 510–523. [CrossRef]
15. Chen, Z.; Jin, X.; Li, L.; Wang, G. A limited-angle ct reconstruction method based on anisotropic tv minimization. *Phys. Med. Biol.* **2013**, *58*, 2019. [CrossRef]
16. Xie, N.; Chen, Y.; Liu, H. Nonlocal low-rank and total variation constrained PET image reconstruction. In Proceedings of the 2018 24th International Conference on Pattern Recognition (ICPR), Beijing, China, 20–24 August 2018; pp. 3874–3879. [CrossRef]
17. Zhang, H.; Wang, L.; Yan, B.; Li, L.; Xi, X.; Lu, L. Image reconstruction based on total-variation minimization and alternating direction method in linear scan computed tomography. *Chin. Phys. B* **2013**, *22*, 078701. [CrossRef]
18. Cai, J.; Jia, X.; Jiang, H.G.S.; Shen, Z.; Zhao, H. Cine cone beam ct reconstruction using low-rank matrix factorization: Algorithm and a proof-of-principle study. *IEEE Trans. Med. Imaging* **2014**, *33*, 1581–1591. [CrossRef] [PubMed]
19. Goldstein, T.; Osher, S. The split Bregman algorithm for L1 regularized problems. *SIAM J. Imaging Sci.* **2009**, *2*, 323–343. [CrossRef]
20. Cai, J.; Osher, S.; Shen, Z. Split Bregman methods and frame based image restoration. *Multiscale Model. Simulation A SIAM Interdiscip. J.* **2009**, *8*, 337–369. [CrossRef]
21. Esser, E. Applications of Lagrangian-based alternating direction methods and connections to split Bregman. *CAM Rep.* **2009**, *9*, 31.
22. Tai, X.; Wu, C. Augmented Lagrangian method, dual methods and split Bregman iteration for ROF model. *Scale Space Var. Methods Comput. Vis.* **2009**, *5567*, 502–513.
23. Dong, W.; Li, X.; Zhang, L.; Shi, G. Sparsity-based image denoising via dictionary learning and structural clustering. In Proceedings of the 2011 IEEE Conference on Computer Vision and Pattern Recognition(CVPR), Colorado Springs, CO, USA, 20–25 June 2011; pp. 457–464. [CrossRef]

24. Dong, W.; Shi, G.; Li, X.; Ma, Y.; Huang, F. Compressive sensing bia nonlocal low-rank regularizaiton. *IEEE Trans. Image Process.* **2014**, *23*, 3618–3632. [CrossRef] [PubMed]
25. Sagheer, S.; George, S. Denoising of low-dose CT images via low-rank tensor modelling and total variation regularization. *Artif. Intell. Med.* **2019**, *94*, 1–17. [CrossRef] [PubMed]
26. Xu, N.; Hou, H.; Cheng, Z.; Wang, M.; Wang, Y.; Wang, G. Nonlocal low-rank and prior image-based reconstruction in a wavelet tight frame using limited-angle projection data. *IEEE Access* **2021**, *9*, 24616–24628. [CrossRef]
27. Hu, Z.; Nie, F.; Wang, R.; Li, X. Low rank regularization: A review. *Neural Netw.* **2021**, *136*, 218–232. [CrossRef] [PubMed]
28. Li, Y.; Han, D. Framelet perturbation and application to nouniform sampling approximation for Sobolev space. *arXiv* **2017**, arXiv:1707.01325.
29. Shen, Y.; Yang, S.; Yuan, D. d-Refinable (dual) pseudo-splines and their regularities. *Int. J. Wavelets Multiresol. Inf. Process.* **2017**, *15*, 1750002. [CrossRef]
30. Lin, Z.; Chen, M.; Wu, L.; Ma, Y. *The Augmented Lagrange Multiplier Method for Exact Recovery of Corrupted Low-Rank Matrices*; Tech. Rep. UILU-ENG-09-2215; Department of Electrical and Computer Engineering, University of Illinois Urbana-Champaign: Urbana, IL, USA, 2009.